Rare Metal Materials and Engineering
Volume 55, Issue 3, March 2026
Available online at www.rmme.ac.cn

Science Press

Cite this article as: Su Yi, Liu Ruizhe, Ahmad Hilal, et al. In-Flight Heating Process of Cerium Oxide Powders in Radio Frequency Thermal Plasma Considering Thermal Resistance Effect[J]. Rare Metal Materials and Engineering, 2026, 55(03): 581-594. DOI: https://doi.org/10.12442/j.issn.1002-185X.20250101.

ARTICLE

In-Flight Heating Process of Cerium Oxide Powders in Radio Frequency Thermal Plasma Considering Thermal Resistance Effect

Su Yi[1,2], Liu Ruizhe[1], Ahmad Hilal[1], Zhao Peng[2], Jin Xingyue[2], Zhu Hailong[3]

[1] Institute of Theoretical Physics, Shanxi University, Taiyuan 030006, China; [2] Institute of Plasma Physics, Hefei Institutes of Physical Science, Chinese Academy of Sciences, Hefei 230031, China; [3] School of Physics and Electronic Engineering, Shanxi University, Taiyuan 030006, China

Abstract: The in-flight heating process of cerium dioxide (CeO_2) powders was investigated through experiments and numerical simulations. In the experiment, CeO_2 powder (average size of 30 μm) was injected into radio-frequency (RF) argon plasma, and the temperatures were measured using a DPV-2000 monitor. A model combining the electromagnetism, thermal flow, and heat transfer characteristics of powder during in-flight heating in argon plasma was proposed. The melting processes of CeO_2 powders of different diameters, with and without thermal resistance effect, were investigated. Results show that the heating process of CeO_2 powder particles consists of three main stages, one of which is relevant to a dimensionless parameter known as the Biot number. When the Biot value≥0.1, thermal resistance increases significantly, especially for the larger powders. The predicted temperature of the particles at the outlet (1800–2880 K) is in good agreement with the experimental result.

Key words: RF thermal plasma; thermal resistance effect; heating process; Biot number

1 Introduction

Radio-frequency (RF) thermal plasma is widely used in plasma spraying and manufacturing of spherical dense powders[1-4] due to its high-temperature (approximately 10 000 K) [5–7] and high-enthalpy (tens of MJ) [8–10]. Plasma spraying involves several processes: injection of a large amount of powder into thermal plasma, powder heating, and impact on substrate. This process has been widely used to prepare metal/ceramic coatings, during which the characteristics of powders have a significant impact on the coating and spheroidization processes[11]. Plasma spheroidization involves the injection of raw powders into plasma, powder heating, and formation of spherical droplets as a result of surface tension through melting. When the molten droplets fly out of plasma, they are solidified into spherical powders due to rapid quenching. The melting process of powders during both the plasma spheroidization and plasma spraying processes is crucial to form good spherical powders[12]. The melting process is based on the in-flight heating of powder particles in plasma, which has already been numerically simulated[13–16]. Most models used a lumped thermal analysis for powders without considering the influence of internal thermal resistance of powders on the heating process. However, the internal thermal resistance of powders is important to the internal temperature distribution of the powders for fully understanding the particle heating behavior, especially for ceramic powders. A more rigorous solution should consider the effect of temperature distribution within the powders[17].

For metal powders, due to their high thermal conductivity, the internal conduction is fast, and temperature variations within the particles can be ignored. Chen et al[18] investigated

Received date: March 03, 2025
Foundation item: National Natural Science Foundation of China (11875039); Shanxi Scholarship Council of China (2023-033); Fundamental Research Program of Shanxi Province (202303021221071); China Baowu Low Carbon Metallurgical Innovation Foundation (2022); 2023 Anhui Major Industrial Innovation Plan Project
Corresponding author: Zhu Hailong, Ph. D., Professor, School of Physics and Electronic Engineering, Shanxi University, Taiyuan 030006, P. R. China, E-mail: zhuhl@sxu.edu.cn; Zhao Peng, Ph. D., Associate Researcher, Institute of Plasma Physics, Hefei Institutes of Physical Science, Chinese Academy of Sciences, Hefei 230031, P. R. China, E-mail: pzhao@ipp.ac.cn

the heating process of tungsten and graphite powders in plasma and proposed a lumped parameter model, which is appropriate for materials with high thermal conductivities. However, for some ceramic powders, their thermal conductivity is low, the heat conduction within the powders is relatively slow, and there is a temperature difference between the particle center and surface[19–21], i. e., when the particle surface melts completely into a liquid phase, the particle interior has not reached its melting point. In plasma spraying, unmelted powders may enhance the kinetic energy dissipation, slowing down the spreading process, and causing particles bouncing off the substrate and splashing[11,22–23]. For the plasma spheroidization process, the unmelted part of the powders may block the plasma torch and affect the spheroidization efficiency of the powders[12,24]. Therefore, it is critical to understand the heating behavior of powders in plasma while considering the thermal resistance effect to improve the plasma spraying and spheroidization processes.

Considering the thermal resistance effect, the Biot number is used to determine the relative importance of heat conduction within particles. Biot number is defined as the ratio of convective heat transfer to conduction heat transfer[25], which is related to particle diameter and trajectory in powder heating. Generally, the larger the particle diameter, the slower the heat transfer rate within particle. This change in heat transfer characteristics will also increase the Biot number. Moreover, the Biot number is also affected by the thermodynamic properties of the plasma around the powders. When powders move through plasma, the surrounding conditions constantly change, leading to variations in the Biot number of the powders during heating. However, the Biot number is usually calculated as an average value during particle heating, and it does not change with the movement of the powders[26]. Although the average value of Biot number can provide a reference to determine whether the thermal resistance should be considered, this approach may deviate from actual experiment conditions and may not fully reflect the internal heating behavior of powders. Therefore, it is important to calculate the variation of Biot number during the particle heating process to gain a more accurate understanding of the heating behavior of powders.

The plasma material preparation process is a multi-parameter technique[27–28]. Numerical modeling is a powerful and cost-effective tool for investigating the heating process of powders. In this research, the heating process with the thermal resistance effect of CeO_2 powders was investigated by a three-dimensional in-flight particle-plasma model[29] and a transient particle heating model. The heating behavior of powders with different diameters and trajectories under the thermal resistance effect was investigated, and the time interval for the complete melting of powders under the thermal resistance effect was determined. Few studies have considered the incorporation of internal thermal resistance of powder into the simulation of the interaction between thermal plasma and ceramic powder. Therefore, this research provides a novel insight, particularly in predicting temperature of powders of different particle sizes in plasma. The results proposed valuable understanding of the heating process of powders in plasma spheroidization and plasma spraying.

2 Experiment

The schematic diagram of the experiment setup is shown in Fig. 1. The experiment system was composed of several key components, including a homemade plasma torch, an RF power supply, a powder feeder, a gas supply system, and a DPV-2000 monitoring instrument (Tecnar Automation Ltd, Canada). Before plasma ignition, argon gas was injected into the plasma torch as a plasma-forming gas. Then, the high-voltage starting device was used to increase the ionization degree of the discharge gas. Subsequently, RF plasma power supply was activated, and the coil current increased, generating and maintaining a stable plasma environment. After the stable plasma was formed, the raw CeO_2 powders were transported to the powder injection probe in the high-temperature region, which was then inserted into the plasma by carrier gas (argon). Simultaneously, the sensing head of the DPV-2000 monitor was positioned at the focal point, which was 100 mm away from the plasma torch nozzle, to continuously monitor the average values of key parameters, including the temperature and velocity of the flying powders. The detailed operational parameters of RF thermal plasma system are listed in Table 1.

3 Model Description

The model is mainly divided into two parts: the in-flight particle-plasma model and the transient particle heating model. In the in-flight particle-plasma model, RF thermal plasma is assumed to be optically thin, and it is in local thermodynamic equilibrium. The thermal plasma flow is calculated by the magnetohydrodynamics theory, using the mass, momentum, and energy conservation equations coupled with Maxwell equations of the electromagnetic field[30]. The discrete phase model is used to calculate the motion trajectory, heat, and mass transfer coupling between the particle phase and the plasma phase. The particles are considered as discrete Lagrangian entities that exchange mass, momentum, and energy with plasma, ignoring the internal thermal resistance effect of powders[29]. Fig. 2a shows the geometric structure of the in-flight particle-plasma model. The dimensions of the plasma torch and chamber are listed in Table 2. The transient particle heating model is established using a relatively simple one-dimensional unsteady heat conduction equation. The model takes into account the internal temperature variation of powders and the solid-liquid phase change during the melting process. The thermodynamic state of plasma around the particle trajectory is calculated using the in-flight particle-plasma model and then loaded into the boundary of the transient particle heating model. Fig. 2b shows the schematic diagram of the transient particle heating model, which involves a spherical computational domain with an initial radius (r_p) during the heating process. The governing

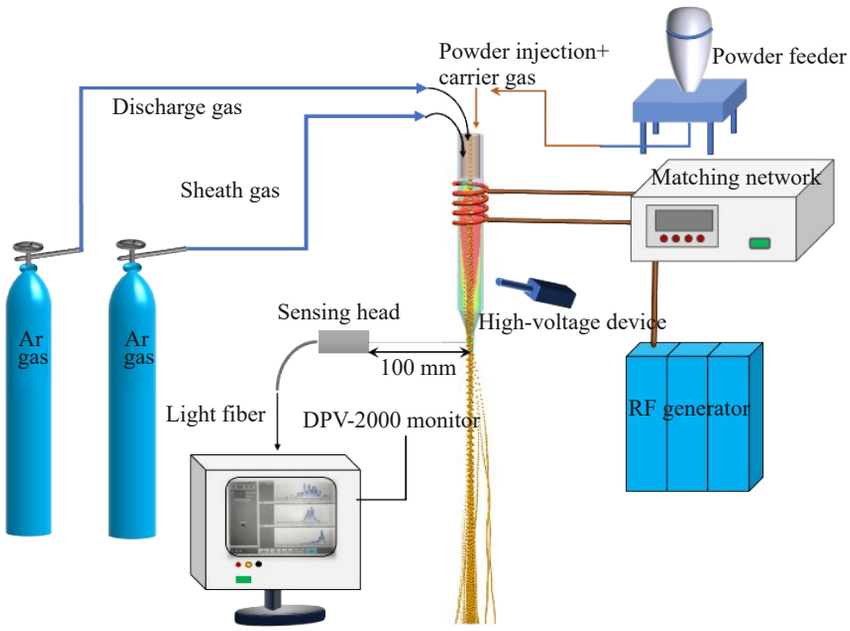

Fig.1 Schematic diagram of experimental setup

Table 1 Experiment conditions for plasma spheroidization of CeO_2 powder

Parameter	Value
Input power/kW	2.0
Flow rate of discharge gas/L·min^{-1}	5.0
Flow rate of sheath gas/L·min^{-1}	25.0
Flow rate of carrier gas/L·min^{-1}	6.0
Feed rate of time-averaged powder/g·min^{-1}	2.0

equations and boundary conditions of the model will be presented below.

3.1 Basic assumptions

(1) Under atmospheric pressure and local thermodynamic equilibrium, the plasma gas around the powders is pure argon, and the electrons and heavy powders are at the same temperature.

(2) Plasma is considered to be an optically thin plasma, so it is not necessary to consider the radiative heat transfer from plasma to powders and the pure argon discharge at atmospheric pressure.

(3) The effect of particle evaporation on plasma is neglected.

(4) Vaporization will not occur until the powders reach the boiling point of the material.

3.2 Governing equation

3.2.1 In-flight particle-plasma model

RF alternating current passes through the coil and generates a strong electromagnetic field in the plasma torch. Argon is ionized by high-speed alternating induced current to form argon plasma. In this process, the alternating electromagnetic field can be controlled by Maxwell equations[31]:

$$\nabla \cdot \boldsymbol{E} = \frac{\rho}{\varepsilon_0} \tag{1}$$

$$\nabla \cdot \boldsymbol{B} = 0 \tag{2}$$

$$\nabla \times \boldsymbol{E} = \frac{\partial \boldsymbol{B}}{\partial t} \tag{3}$$

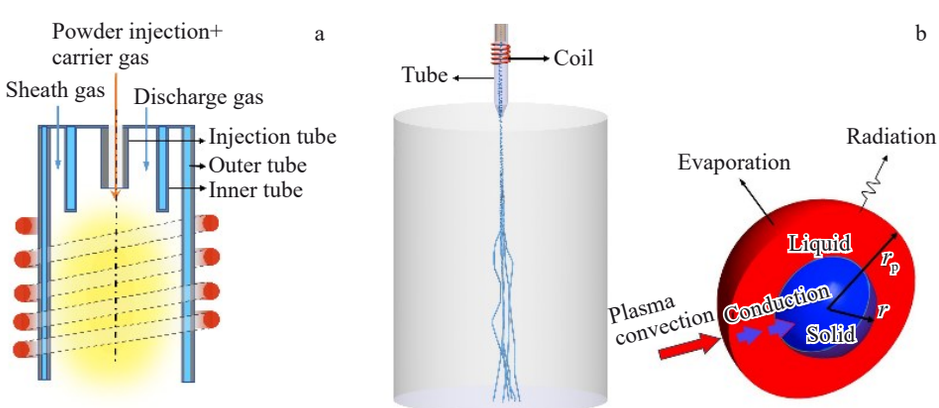

Fig.2 Schematic diagrams of in-flight particle-plasma model (a) and transient particle heating model (b)

Table 2 Dimensions of plasma torch and chamber

Parameter	Value
Inner radius of outer tube/mm	18.0
Outer radius of outer tube/mm	20.0
Length of outer tube/mm	236.0
Inner radius of inner tube/mm	13.0
Outer radius of inner tube/mm	15.0
Length of inner tube/mm	58.0
Inner radius of injection tube/mm	2.0
Outer radius of injection tube/mm	3.0
Length of injection tube/mm	45.0
Chamber radius/mm	40.0
Chamber length/mm	724.0
Coil major radius/mm	25.0
Coil axial pitch/mm	66.0
Coil minor radius/mm	3.0
Number of coil turns	5
Nozzle length/mm	30.0
Nozzle outlet radius/mm	6.0

$$\nabla \times \boldsymbol{B} = \mu_0 \varepsilon_0 \frac{\partial \boldsymbol{E}}{\partial t} + \mu_0 \boldsymbol{J} \tag{4}$$

where $\boldsymbol{E}$ and $\boldsymbol{B}$ are the electric field strength and magnetic induction strength, respectively; ρ is the charge density; ε_0 is the permittivity; μ_0 is the permeability constant; $\boldsymbol{J}$ is the current density. The simplified forms of the Maxwell equations can be expressed in terms of the magnetic vector potential $\boldsymbol{A}$, where the Maxwell equations in coil regions and plasma can be simplified to Eq.(5–6). In addition, considering the fluid properties of RF thermal plasma, the governing equations of plasma flow[32] can be expressed by Eq.(7–9).

$$\nabla^2 \boldsymbol{A} = -\mu_0 \boldsymbol{J} - \mu_0 \varepsilon_0 \omega^2 \boldsymbol{A} \tag{5}$$

$$\nabla^2 \boldsymbol{A} = \mu_0 \sigma \nabla \varphi + (i\omega \mu_0 \sigma - \mu_0 \varepsilon_0 \omega^2) \boldsymbol{A} \tag{6}$$

$$\nabla \cdot (\rho_\infty \boldsymbol{u}) = S_\mathrm{p}^\mathrm{c} \tag{7}$$

$$\nabla \cdot (\rho_\infty \boldsymbol{u}\boldsymbol{u}) = -\nabla P + \nabla \cdot \left[\mu (\nabla \boldsymbol{u} + \nabla \boldsymbol{u}^T) - \frac{2}{3} \mu (\nabla \cdot \boldsymbol{u}) \boldsymbol{I} \right] + \boldsymbol{J} \times \boldsymbol{B} + S_\mathrm{p}^\mathrm{m} \tag{8}$$

$$\nabla \cdot (\rho_\infty \boldsymbol{u} h) = \nabla \cdot \left(\frac{\kappa}{C_\mathrm{p}'} \nabla h \right) + \boldsymbol{J} \cdot \boldsymbol{E} - Q_\mathrm{radiate} + S_\mathrm{p}^\mathrm{E} \tag{9}$$

where μ, $\boldsymbol{u}$, h, κ, ρ_∞, and C'_p represent the plasma viscosity, velocity, enthalpy, thermal conductivity, density, and specific heat, respectively; $\boldsymbol{I}$ is the three-dimensional unit tensor; P is the static pressure; Q_radiate is the radiation energy lost; $\nabla \boldsymbol{u}^\mathrm{T}$ is the transpose of the vector gradient tensor $\nabla \boldsymbol{u}$; S_p^c, S_p^m, and S_p^E are the mass, momentum, and energy transported into plasma by the particles[33–34], respectively; σ is the Stefan-Boltzmann constant; S, φ, and ω are related parameters.

$$S_\mathrm{p}^\mathrm{c} = \sum_{i=1}^{N} \Delta m_i \tag{10}$$

$$S_\mathrm{p}^\mathrm{m} = \sum_{i=1}^{N} \Delta F_i \tag{11}$$

$$S_\mathrm{m}^\mathrm{E} = \sum_{i=1}^{N} \Delta Q_i \tag{12}$$

where Δm_i, ΔF_i, and ΔQ_i represent the mass change, resultant force variation, and heat transfer change of the ith particle interacting with the plasma, respectively; N denotes the total number of particles.

The turbulent effect is considered using the standard k-ε model[14,34]:

$$\nabla \cdot (\rho_\infty \boldsymbol{u} k) = \nabla \cdot \left[\left(\mu + \frac{\mu_\mathrm{T}}{\sigma_k} \right) \nabla k \right] + G_k - \rho_\infty \varepsilon \tag{13}$$

$$\nabla \cdot (\rho_\infty \boldsymbol{u} \omega) = \nabla \cdot \left[\left(\mu + \frac{\mu_\mathrm{T}}{\sigma_\varepsilon} \right) \nabla \omega \right] + C_{1\varepsilon} \frac{\varepsilon}{k} G_k - C_{2\varepsilon} \rho_\infty \frac{\varepsilon^2}{k} \tag{14}$$

where ρ_∞ is plasma density; k is the turbulence kinetic energy; ε is the turbulent dissipation; μ_T is the turbulent viscosity; G_k is the generation of turbulence kinetic energy; $C_{1\varepsilon}$, $C_{2\varepsilon}$, σ_k, and σ_ε are constants set as 1.44, 1.92, 0.25, and 1.0, respectively.

A powder particle is considered as a discrete Lagrangian entity that exchanges mass, momentum, and energy with plasma. From Newton's second law, momentum variation for a particle[12,14,19] can be described as follows:

$$F_\mathrm{p} = F_\mathrm{D} + F_\mathrm{g} + F_\mathrm{b} \tag{15}$$

$$F_\mathrm{D} = \frac{\pi d_\mathrm{p}^{\,2}}{8} \rho_\infty C_\mathrm{D} \left| \boldsymbol{u} - \boldsymbol{v}_\mathrm{p} \right| (\boldsymbol{u} - \boldsymbol{v}_\mathrm{p}) \tag{16}$$

$$F_\mathrm{g} = \rho_\mathrm{p} g V_\mathrm{p}, \quad F_\mathrm{b} = \rho_\infty g V_\mathrm{p} \tag{17}$$

where F_p is the resultant force acting on particles; F_D, F_g, and F_b are the force, gravitational force, and buoyancy force, respectively; C_D is the drag coefficient[35]; g is the gravitational acceleration; d_p, $\boldsymbol{v}_\mathrm{p}$, ρ_p, and V_p represent the diameter, velocity, density, and volume of particle, respectively. Therefore, the equation of motion for individual particle in the plasma flow is given as follows:

$$\rho_\mathrm{p} \frac{\mathrm{d}\boldsymbol{v}_\mathrm{p}}{\mathrm{d}t} = \left(\frac{3\rho_\infty C_\mathrm{D}}{4 d_\mathrm{p}} \right) \left| \boldsymbol{u} - \boldsymbol{v}_\mathrm{p} \right| (\boldsymbol{u} - \boldsymbol{v}_\mathrm{p}) + g (\rho_\mathrm{p} - \rho_\infty) \tag{18}$$

3.2.2 Transient particle heating model

The calculations of the particle temperature during its trajectory in plasma are conducted based on the energy balance on the particle. The net energy Q_n, which contributes to the heating or cooling of the particle, is the difference between the heat received by the particle from plasma by conduction and convection (Q_cv) and the heat lost from the particle surface by radiation to the surroundings (Q_rad)[12,36].

$$Q_\mathrm{n} = Q_\mathrm{cv} - Q_\mathrm{rad} \tag{19}$$

$$Q_\mathrm{cv} = A h_\mathrm{c} \left(T_\infty - T_\mathrm{p} \right) \tag{20}$$

$$Q_\mathrm{rad} = A \sigma \varepsilon \left(T_\mathrm{p}^4 - T_\mathrm{a}^4 \right) \tag{21}$$

where A is the surface area of the powders; T_∞ and T_p represent the plasma temperature and particle temperature, respectively; ε is the emissivity of the object related to the surface state and material properties of the object; T_a is the ambient temperature; h_c is the surface heat transfer coefficient related to both particle diameter and plasma flow field. The value of

h_c can be expressed by the form of Nusselt number:

$$h_c = \frac{\kappa Nu}{d_p} \tag{22}$$

where Nu is the Nusselt number. The Nusselt number is based on the similarity principle in the study of convective heat transfer, and it is calculated as follows:

$$Nu=2.0+0.6Re^{1/2}Pr^{1/3} \tag{23}$$

where Pr and Re are the Prandtl number and the Reynolds number, respectively. Pr and Re can be expressed as follows:

$$Pr = \frac{C_p'\mu}{\kappa}, \quad Re = \frac{\rho_\infty d_p \left| u - v_p \right|}{\mu} \tag{24}$$

Thermal resistance must be considered for ceramic materials with low thermal conductivity. The heat transfer in spherical particles can be determined by the following one-dimensional unsteady heat conduction equation.

$$\rho_p C_p \frac{\partial T_p}{\partial t} = \frac{1}{r^2}\frac{\partial}{\partial r}\left(r^2 \kappa_p \frac{\partial T_p}{\partial r}\right) \tag{25}$$

where ρ_p, C_p, and κ_p are the density, specific heat, and thermal conductivity of powders, respectively; r is powder size. A good estimate of the relative importance of the internal heat conduction within the particle can be proposed based on the Biot number[25]. The mathematical expression for the Biot number (Bi) used in this research is as follows:

$$Bi = \frac{h_c d_p}{\kappa_p} \tag{26}$$

When the Biot number is small, internal conduction is relatively fast, and the temperature variations within the particle can be neglected. When the Biot number is large, the temperature change inside the particle cannot be ignored. In this case, the thermal resistance effect should be considered into the one-dimensional unsteady heat conduction equation.

Powders are heated continuously in plasma to their melting point, and a solid-liquid phase transition occurs. For this melting process, the mushy region model is introduced[37]. The enthalpy (H) of a material can be expressed as the sum of sensible heat and latent heat, as follows:

$$H=h+\Delta H \tag{27}$$

where h is the apparent enthalpy and ΔH is the latent heat of phase change. The latent heat of phase change during the melting process of powders can be expressed as follows:

$$\Delta H = x_s(T) L_m \tag{28}$$

where L_m is the latent heat of fusion of particle material; x_s is the liquid phase fraction; T is temperature. $x_s(T)$ can be written as follows:

$$x_s(T) = \begin{cases} 0 & T \leqslant T_{solidus} \\ \dfrac{T - T_{solidus}}{T_{liquidus} - T_{solidus}} & T_{solidus} < T < T_{liquidus} \\ 1 & T \geqslant T_{liquidus} \end{cases} \tag{29}$$

where $T_{solidus}$ and $T_{liquidus}$ are the solidus temperature and liquidus temperature of particles, respectively.

Therefore, the governing equations for the heating, melting, and evaporation of particles throughout their trajectories in plasma[12,28,37] can be summarized, as follows:

$$\frac{dT_p}{dt} = \frac{6Q_n}{\rho_p \pi {d_p}^3 C_p} \quad T_p < T_m \tag{30}$$

$$\frac{dx_s}{dt} = \frac{6Q_n}{\rho_p \pi {d_p}^3 L_m} \quad T_p = T_m \tag{31}$$

$$\frac{dT_p}{dt} = \frac{6(Q_n)}{\rho_p \pi {d_p}^3 C_p} \quad T_m < T_p < T_b \tag{32}$$

$$\frac{dd_p}{dt} = \frac{6(Q_n)}{\rho_p \pi {d_p}^3 L_v} \quad T_p = T_b \tag{33}$$

where T_m, T_b, and L_v are the melting point, boiling point, and latent heat of evaporation of particles, respectively.

3.3 Calculation method and boundary conditions

Fig.2a shows the geometry structure of the in-flight particle-plasma model. The temperature of the water-cooled tube and chamber walls was set as 300 K. The velocity of the tube wall satisfies a non-slip velocity boundary condition, and the magnetic vector potential at the boundary of the extended region conforms to the far-field boundary condition. Table 3 summarizes these boundary conditions, where v_{in} is the injection rate of carrier gas, sheath gas, and discharge gas. The thermodynamic and transport properties of the thermal plasma are fitted as a nonlinear function of temperature[36]. The powders are axially released from the carrier gas inlet, following a Rosin-Rammler particle size distribution function[38–40]. The detailed geometrical structure of the in-flight particle-plasma model and boundary conditions are described in Ref. [12]. The second-order upwind scheme is used to discretize the governing equations, and SIMPLE algorithm based on pressure and velocity coupling is used for iterative calculation. The standard k-ε model is used to calculate the turbulence effect in the downstream region.

The particle heating process in plasma was calculated using the Lagrangian calculation model, which involves computing the micro-trajectories of each particle within a time interval[41]. Powders are treated as individual entities

Table 3 Boundary conditions for RF thermal plasmas

Property	Inlet	Outlet	Tube	Chamber	Outside
Velocity, v/m·s^{-1}	v_{in}	$(\frac{\partial v}{\partial z})\|_{outlet} = 0$	0	0	0
Temperature, T/K	300	$(\frac{\partial T}{\partial z})\|_{outlet} = 0$	300	300	300
Value of magnetic vector potential, A	0	$(\frac{\partial \boldsymbol{A}}{\partial z})\|_{outlet} = 0$	Coupled boundary	$(\frac{\partial \boldsymbol{A}}{\partial z})\|_{chamber} = 0$	0

with three specific parameters: temperature, injection position, and injection timing. Additionally, at each time step in the thermal plasma flow calculation, particle conditions, such as diameter, position, velocity, and temperature, along with source terms for the flow calculation, require updating. Subsequently, the thermal plasma flow at specific timing is calculated through iterative processes using the obtained source terms. The particle velocity is determined from the previous step, and the Reynolds number can be calculated using Eq.(24). The new particle velocity is then obtained by solving Eq.(15), and the temperature at the next moment for the same particle is calculated by Eq. (19). Particle trajectories, velocities at each time step, and particle temperatures are determined through iterative computational cycles. Fig.3 shows the schematic diagram of the Lagrangian model to calculate the heating behavior of in-flight particle, namely the calculation process of particle velocity, trajectory, and temperature in the program.

$$T_{\mathrm{p}}^{i+1}=T_{\mathrm{p}}^{i}+Q_{\mathrm{n}}\Delta t \tag{34}$$

$$u_{\mathrm{p}}^{i+1}=u_{\mathrm{p}}^{i}+\frac{F_{\mathrm{p}}\Delta t}{m_{\mathrm{p}}^{i}} \tag{35}$$

$$x_{\mathrm{p}}^{i+1}=x_{\mathrm{p}}^{i}+u_{\mathrm{p}}^{i}\Delta t \tag{36}$$

where T_{p}^{i+1} and T_{p}^{i} are the temperature of the particle at time t^{i+1} and t^{i}, respectively; $m_{\mathrm{p}}{}^{i}$ is the mass of the particle at time t^{i}; x_{p}^{i+1} and x_{p}^{i} are the positions of the particle at time t^{i+1} and t^{i}, respectively; u_{p}^{i+1} represents the average velocity of the particle in the time range Δt; Q_{n} is the net energy that particles receive from the plasma.

For the transient particle heating model, the first layer mesh size near the surface of the calculation domain is 0.0001 mm, which gradually increases with the increase in radial distance of the grid point. The calculation domain is divided into structured grids with size of 0.001 mm. Based on the preliminary calculation results, the calculation domain is set to d_{p}=0.030 mm. During the calculation of powders of different diameters, the scaling function in FLUENT software is used to obtain the desired size model. The thermodynamic state of plasma along the particle path is calculated in the calculation domain of particle trajectory, and the exported data are loaded into the boundary of the calculation domain of particle thermal resistance. The initial temperature at the beginning of the calculation is as follows:

$$T(r)=T_0=300\ \mathrm{K}\ (t=0) \tag{37}$$

The boundary condition at the center of the particle is as follows:

$$\left(\frac{\partial T}{\partial r}\right)\Big|_{r=0}=0 \tag{38}$$

When the boiling point (T_{v}) or melting point (T_{m}) of the powders is reached, Eq.(39) can be obtained, as follows:

$$T_{\mathrm{s}}=T_{\mathrm{m}},\quad T_{\mathrm{s}}=T_{\mathrm{v}} \tag{39}$$

where T_{s} is the surface temperature of powders. The unsteady heat conduction relaxation time is approximately 1 μs for a particle under various plasma conditions[42]. In this study, CeO_2 powders with initial diameter of 15, 30, 50, and 60 μm were calculated in argon thermal plasma using a fixed time step of 1–10 μs. Table 4 shows the thermophysical properties of CeO_2 powder used in the calculation. The three-dimensional model was implemented within the framework of the commercial computational fluid dynamics (CFD) software FLUENT, and the electromagnetic field was treated by a grid extending outside the plasma region[43]. A user-defined scalar technique was used to customize the basic C++ code to add Maxwell's equations into its built-in fluid dynamics module. The discrete phase model was used to calculate the powders, and the force and heat transfer of discrete phase powders in plasma were controlled by several user-defined functions of C++ codes[29]. Finally, the calculation results were imported into post-processing software for visual analysis.

4 Results and Discussion

4.1 In-flight heating of powder in RF thermal plasma

It is found that the efficient melting of powders in RF

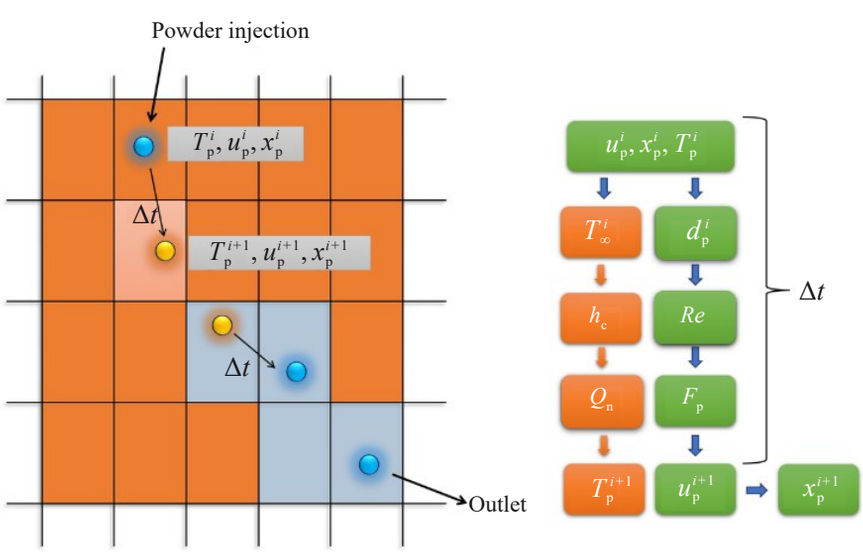

Fig.3 Schematic diagram of calculation process of particle velocity, trajectory, and temperature

Table 4 Thermophysical properties of CeO_2 powder

Thermophysical property	Value
Density/kg·m^{-3}	7130
Melting point/K	2443
Boiling point/K	2880
Specific heat of solid/J·kg^{-1}·K^{-1}	460
Specific heat of liquid/J·kg^{-1}·K^{-1}	510
Latent heat of fusion/×10^5 J·kg^{-1}	4.62
Latent heat of vaporization/×10^6 J·kg^{-1}	1.248
Thermal conductivity/W·m^{-1}·K^{-1}	12

plasma is important for plasma-based powder processing technique. The heating of powders depends on the amount of heat transfer and motion of the powders in the plasma, which is related to the temperature distribution of the plasma. Fig.4a shows the three-dimensional temperature distribution of the plasma. The temperature distribution exhibits non-uniformity. The peak of plasma temperature is about 10 000 K, which occurs in the coil region. The temperature of plasma downstream and chamber regions derived from convection and conduction is progressively decreased along with plasma flow[14]. The non-uniform temperature distribution has a significant influence on the particle heating process. Fig. 5a depicts the three-dimensional trajectory of powders injected into the plasma. Due to the non-uniform plasma temperature distribution, powders injected into the plasma will have different heating histories and heating time. Generally, a long residence time of powder in plasma is expected, because it can lead to effective heating and melting of the powders. The residence time of the powders in the plasma is significantly affected by their in-flight velocity, and the slower particle velocity ensures that the powders have a longer residence time in the plasma. The maximum particle velocity is 30 m/s, which is measured near the nozzle of the plasma torch, as shown in Fig.5b.

The in-flight heating histories of powder in plasma can be roughly divided into three stages, as shown in Fig. 6. In the first stage, surface powders are heated from room temperature to the melting point in a very short time interval by absorbing plasma energy. Subsequently, the powders are melted into droplets depending on the particle size. Some small droplets may be completely melted or even evaporated, whereas large droplets may only be partially melted[14,44]. These two stages together constitute the heating stage of the particles. In the third stage, when powders fly out of the plasma area, the particle temperature rapidly decreases, causing the powders to solidify and form spherical powder under the action of surface tension. The heating and solidification time of the particles is approximately 14.5 and 149.6 ms, respectively. Considering the thermal resistance of CeO_2 powders with low thermal conductivity, the heating process of the powder particles from the surface to the

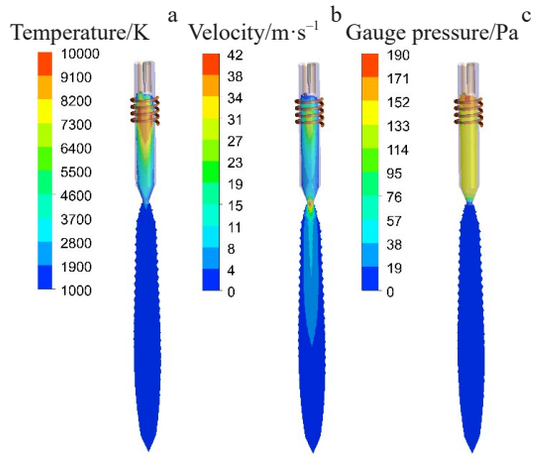

Fig.4 Three-dimensional temperature distribution (a), velocity distribution (b), and gauge pressure distribution (c) of plasma

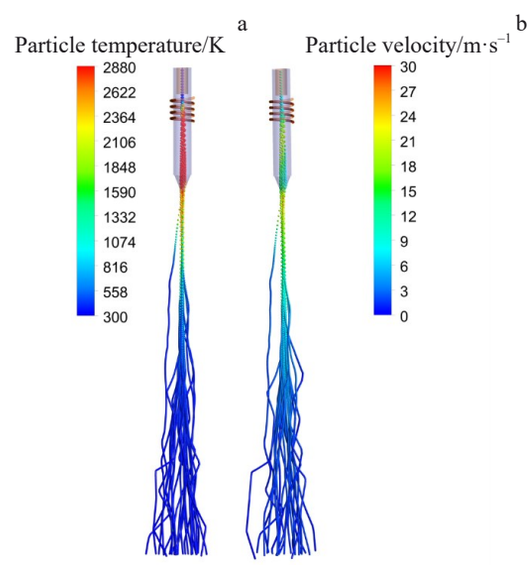

Fig.5 Three-dimensional trajectory of powders injected into plasma (a); variation of particle velocity along their motion trajectories (b)

interior is longer than that of metal powders with high thermal conductivity[19,21]. Fig.7 shows the schematic diagram of the internal heat transfer mechanism of CeO_2 powder during heating stage. When a particle enters the thermal plasma, its surface is initially heated by convective heat transferred from the plasma. Subsequently, the heat is transferred from the surface of the particle to its interior through thermal conduction, causing the internal temperature to gradually rise. Due to the thermal resistance effect, a temperature gradient will be formed between the interior and surface of the particles.

4.2 Effect of powder diameter on heating process

The temperature gradient inside powders during the in-flight heating in plasma largely depends on the diameter of powders. The initial powder diameter of 64, 50, 30, and 15 μm was used to investigate the effect of powder diameter on the heating process of particles.

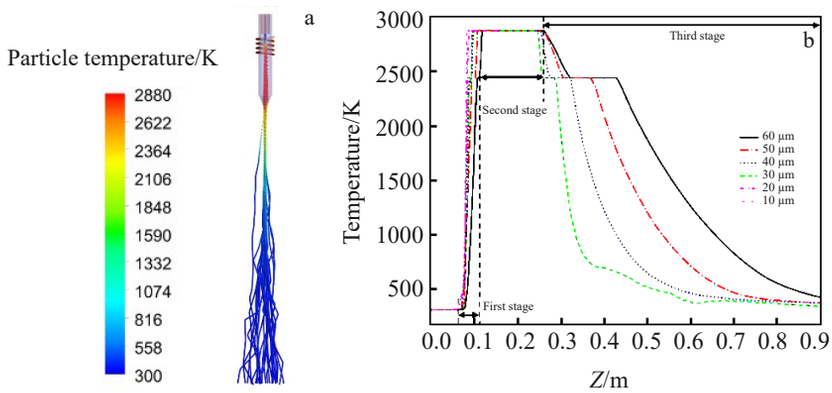

Fig.6 Three-dimensional in-flight heating histories of powder in plasma (a); in-flight heating histories of powders of different particle diameters along *Z* direction (b)

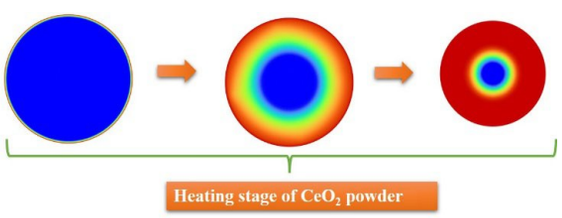

Fig.7 Schematic diagram of internal heat transfer mechanism of CeO_2 powder during heating stage

Fig. 8 illustrates the variation in surface and center temperatures of CeO_2 powders when they are heated from room temperature to boiling point. As shown in Fig.8a–8b, the first heating stage for powders of larger particles (64 and 50 μm) lasts for about 5 ms with a negligible difference. Furthermore, in the second heating stage, the temperature difference between the surface and the center of the powder particles is significant, indicating that the surface is about to boil while the center temperature remains at the melting point. Fig. 8c – 8d reveal the heating characteristics of smaller-sized particles (30 and 15 μm). The time required for the surface temperature to reach the melting point is shorter than that of large-sized powders, and the temperature gradient between the surface and the center is significantly reduced, especially for the powders with particle size of 15 μm.

According to the heat transfer principle, the heating process of powders of different particle sizes is related to a dimensionless parameter, namely the Biot number, which is defined as the ratio of heat convection from the particle surface to thermal conduction from the particle interior[25], as expressed in Eq.(26). When the Biot number is high, it means

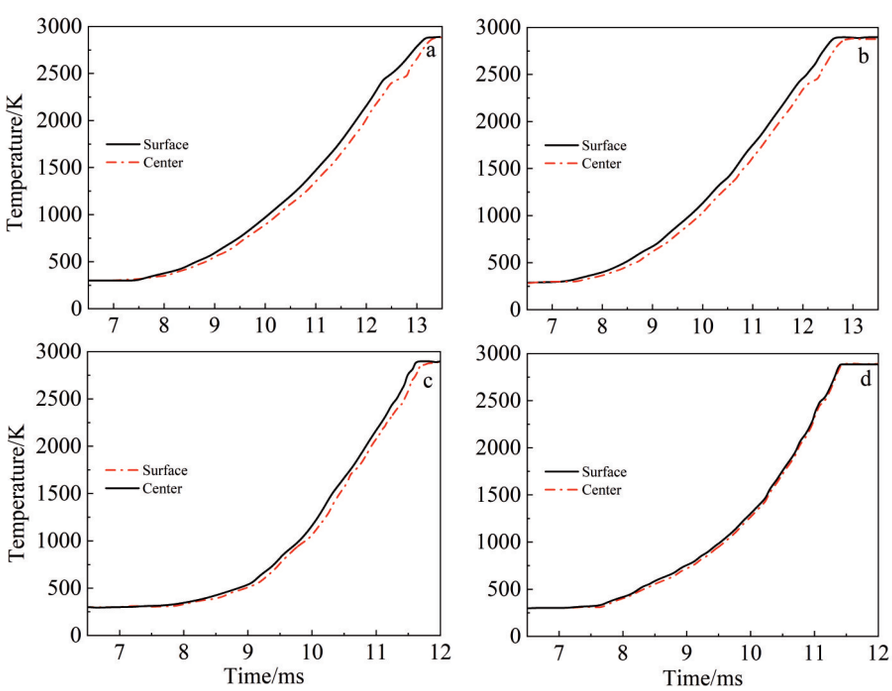

Fig.8 Surface and center temperatures of CeO_2 powders of different initial powder diameters: (a) 64 μm, (b) 50 μm, (c) 30 μm, and (d) 15 μm

that the heating effect of the plasma on the material surface is significantly stronger than the internal heat conduction. This result causes a rapid accumulation of external heat on the surface of powders, whereas the internal heat transfer is relatively slow, which aggravates the temperature gradient between the surface and the interior. As shown in Fig. 9, the temperature difference of the powders becomes obvious when the Biot number is close to 0.1. It is worth noting that in the initial stage of heating, since the Biot number is much lower than 0.1, the surface and center regions of the powders have nearly identical temperatures with a very small temperature difference. However, as the powders move through the plasma, the surrounding conditions continue to change. This dynamic environment directly affects the Biot number of the powders during the heating process. As shown in Fig. 9, when the powders of either large size (64 and 50 μm) or small size (30 and 15 μm) are heated within the plasma, the surrounding environment parameters change, reflecting the dynamic changes in the Biot number. For the powders of 64 and 50 μm in particle diameter, the Biot number changes significantly during the heating process, and it (greater than 0.1) can also result in a temperature difference of up to 200 K between the surface and center of the particles. as shown in Fig. 9a – 9b. Consequently, the heat conduction mechanism within the powders becomes significant and must be taken into account. It is worth noting that CeO_2 powders of particle size of 15 μm have a low Biot number of less than 0.03 throughout heating process, indicating the minimal thermal resistance in the plasma in this research. To further quantify the relationship between particle size and Biot number, the time-averaged Biot number was calculated under different particle size conditions, and the results are shown in Fig. 10. It can be seen that the time-averaged Biot number is increased with the increase in particle size. The time-averaged Biot number is only 0.015 when the particle size is 15 μm and it reaches 0.078 when the particle size reaches 64 μm.

4.3 Melting behavior of powder in RF thermal plasma

Investigating the efficient melting mechanism of powders in a plasma environment is crucial in plasma-based powder processing technique. Once the surface temperature of the powder particles reaches their melting point, there is a short pause in the process. During this stage, the majority of the thermal energy is consumed in overcoming the latent heat of fusion[15]. When the powder particle temperature reaches its melting point, the thermal resistance effect causes the particle surface to melt, resulting in the formation of a liquid film on the particle surface. Subsequently, the heat is conducted from the particle surface towards the center region. Fig. 11 illustrates the quantitative heat transfer from the particle surface to the interior of CeO_2 particle of 50 μm in size during melting process, where t is the time after the powders are injected into plasma and D is the radius of the solid phase. During the particle melting process, the liquid fraction varies from 0.00 to 1.00 according to Eq. (29), resulting in a mushy region at the interface between the solid and liquid phases, namely a transition region, with the liquid phase fraction ranging from 0.00 to 1.00, as shown in Fig. 11d. In the melting process, CeO_2 particles are transformed from solid phase (represented by blue) to liquid phase (represented by red). Once the particles are completely melted, the liquid fraction becomes 1.00. The particle starts to melt at t=11.95 ms and becomes completely liquid after about 0.35 ms. In this study,

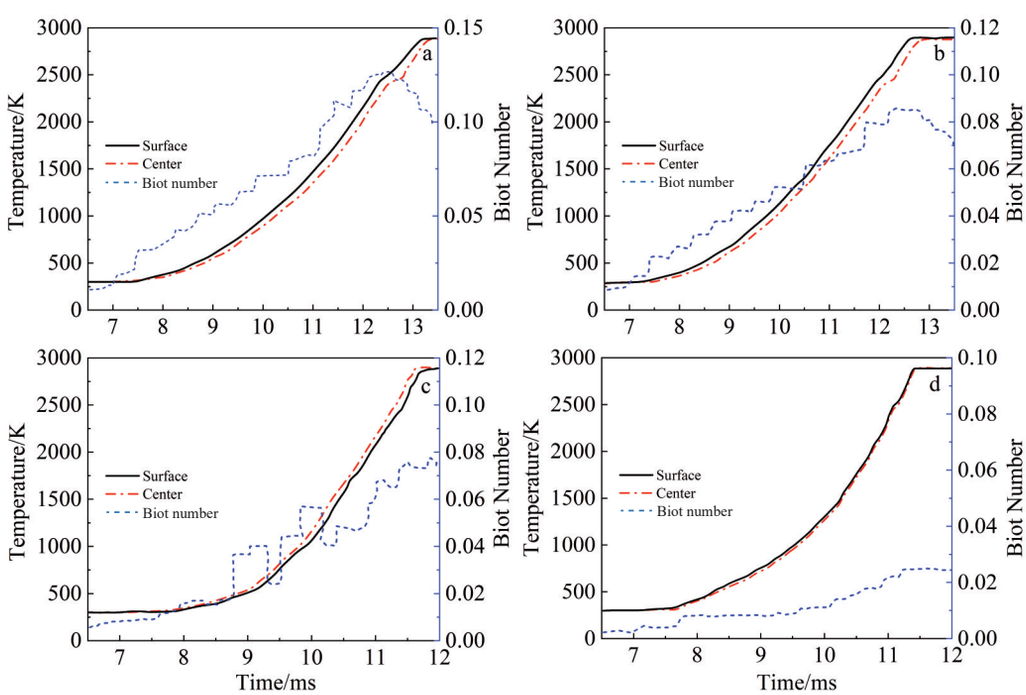

Fig.9 Temperature variations at surface and center as well as Biot number of CeO_2 powders of different initial diameters during heating: (a) 64 μm, (b) 50 μm, (c) 30 μm, and (d) 15 μm

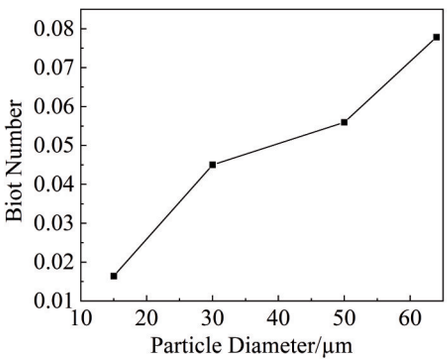

Fig.10 Time-averaged Biot number variation with particle diameter of powders

considering the computational efficiency and the maximum mesh size of 0.001 mm, particles are considered completely melted when the radius of the solid phase reaches 0.5 μm.

Accurate prediction of the complete melting time of the particles is of great significance in powder processing and material preparation[45–46]. To compare and validate the accuracy of the transient particle heating model, a theoretical melting time formula[11] was used: $\Delta t_{melt}=(1+2/Bi)r_p^2\rho_pL/6\kappa_p(T_\infty-T_m)$[11]. The results from Ref. [11] and obtained by the model in this research are shown in Fig. 12, where R^* is a dimensionless quantity to describe the melting radius of CeO_2 powders with the expression of $R^*=(r_p-r_m)/r_p$. In this case, r_m is the radius of the solid phase. It can be seen that these results are in good agreement, especially for the powders with diameter of 15 μm. For powders with diameter of 50 and 64 μm, there is a certain difference between the calculation results, which may be because the calculations in Ref. [11] neglect the temperature distribution within the solid phase during the melting process. For small particles, the surface and center temperatures are very similar. Large particles (size of 50 and 64 μm) have significant temperature differences between the surface and center regions, so the solid phase temperature distribution cannot be ignored. Therefore, the melting time of the powders obtained in this research is longer than that from Ref. [11]. The simulations provide more accurate predictions for powders of larger particle size and higher thermal resistance.

4.4 Comparison of powder behavior between calculation and experiment results

Based on the abovementioned model, the in-flight heating histories of powders in plasma under the experiment conditions were predicted, as shown in Fig. 13a. Fig. 13b shows the temperature distribution of CeO_2 particles at the nozzle outlet. On the *X*-*Y* plane, the majority of particles are heated to the melting point, and they are mainly concentrated at the nozzle center. The histogram of temperature distribution is shown in Fig. 14a. The results show that the temperature of CeO_2 particles at the nozzle outlet ranges from 1800 K to 2880 K, which is consistent with temperature monitoring results obtained using DPV-2000, as shown in Fig. 14b. The temperature distribution of particles exhibits good Gaussian distribution characteristics, indicating that the temperature of the majority of particles in the plasma is within a relatively concentrated range.

During the heating process, when the particles reach the boiling point of the material, their sizes begin to decrease. When some small particles enter the plasma core, in particular, their sizes rapidly decrease, or even they completely evaporate, as shown in Fig. 15a. The diameter distribution of CeO_2 particles at nozzle outlet is shown in Fig. 15b. Fig. 16a and 16b show the diameter distribution histograms of

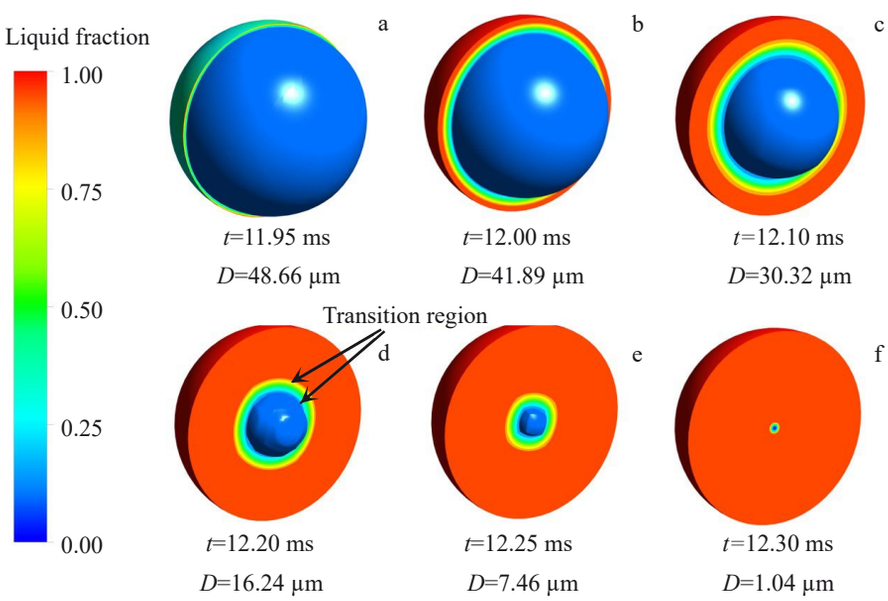

Fig.11 Schematic diagrams of melting process of CeO_2 particle with diameter of 50 μm: (a) *t*=11.95 ms; (b) *t*=12.00 ms; (c) *t*=12.10 ms; (d) *t*=12.20 ms; (e) *t*=12.25 ms; (f) *t*=12.30 ms

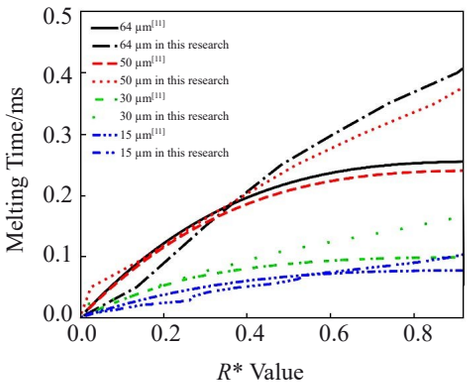

Fig.12 Comparison of melting time of powders of different particle diameters in plasma by different calculation models

simulated and experimentally measured CeO_2 particles, respectively. Comparative analysis indicates that the measured particle size distribution is consistent with the simulated particle size distribution for large particles (diameter>25 μm). Since the evaporation diameter of small particles is set to 0.1 nm and the DVP-2000 device is insensitive to smaller particles, inferior matching of diameter variation of the small particles (size<25 μm) occurs. The calculated average particle size of 26 μm is quite close to the experimentally measured value (24 μm). The velocity distribution analysis of particles at the nozzle outlet is shown in Fig.17. On the *X*-*Y* plane, the high-speed particles are primarily concentrated at the center of the nozzle. The histogram of the simulated particle velocity distribution is shown in Fig. 18a. The results show that the particle velocity presents the Gaussian distribution, which is consistent with the experimentally measured CeO_2 velocity distribution, as shown in Fig.18b.

From the results of experiments and simulations, it can be seen that most particles can be effectively melted during in-flight heating in plasma. It is found that the complete melting of particles during in-flight heating in plasma promotes the formation of spherical powder. Fig. 19 shows the microstructure of CeO_2 powder processed in RF thermal plasma under experiment conditions. The majority of particles with size smaller than 30 μm appear to melt and form well-defined spherical shapes. However, for the larger particles, only their surfaces melt, and the entire particle cannot be completely melted under the experiment conditions in this

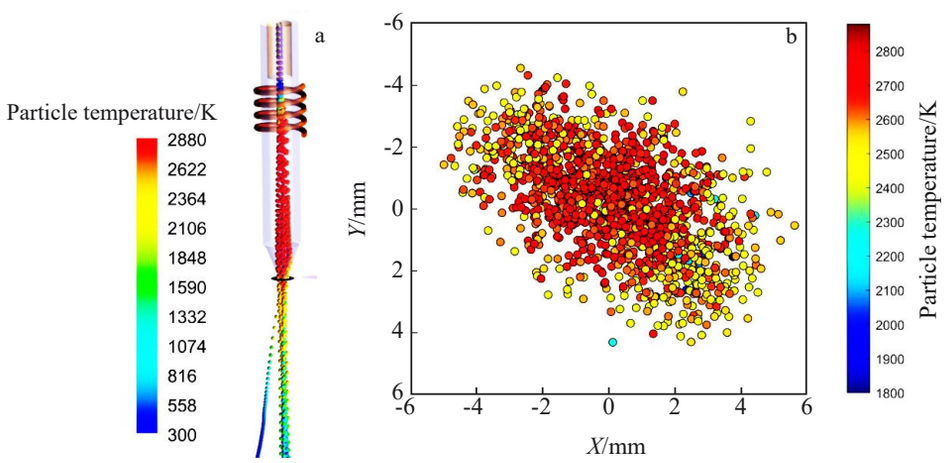

Fig.13 Temperature variation of CeO_2 particles in plasma (a); temperature distribution of CeO_2 particles at nozzle outlet (b)

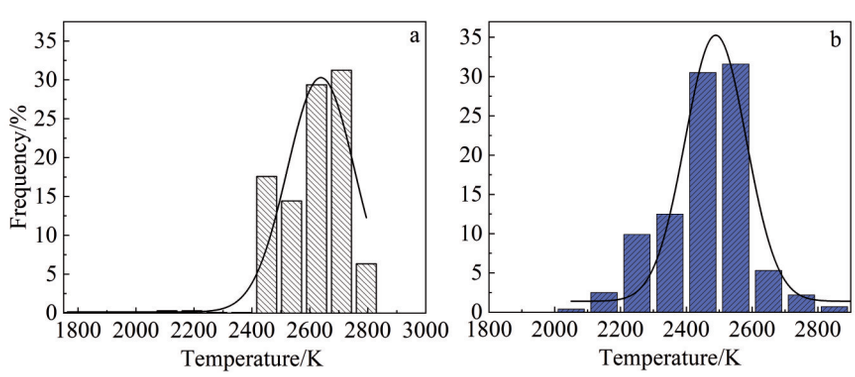

Fig.14 Temperature distribution histograms of CeO_2 particles at nozzle outlet: (a) numerical calculations and (b) experiment measurements

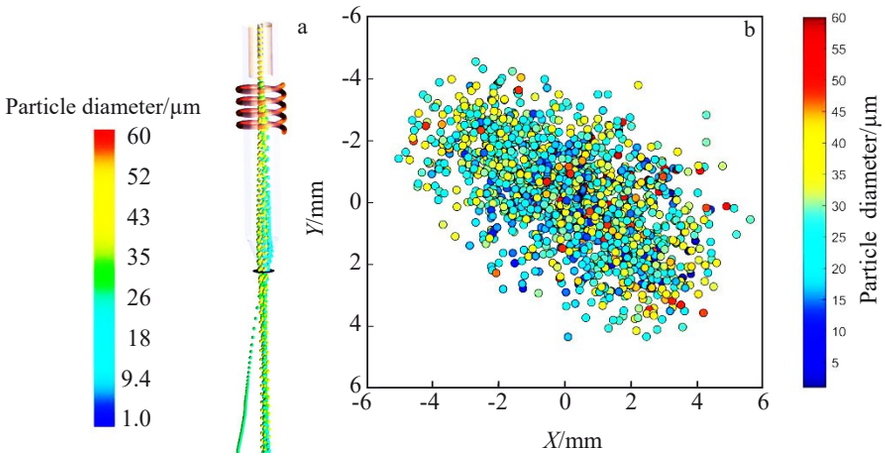

Fig.15 Diameter variation of CeO_2 particles in plasma (a); diameter distribution of CeO_2 particles at nozzle outlet (b)

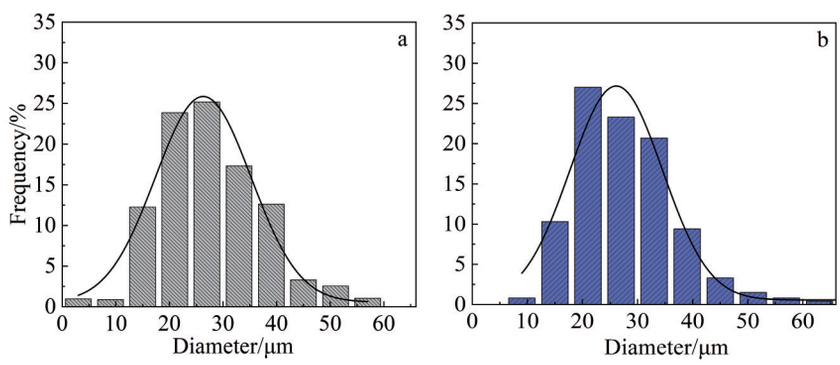

Fig.16 Diameter distribution histograms of CeO_2 particles at nozzle outlet: (a) numerical calculations and (b) experiment measurements

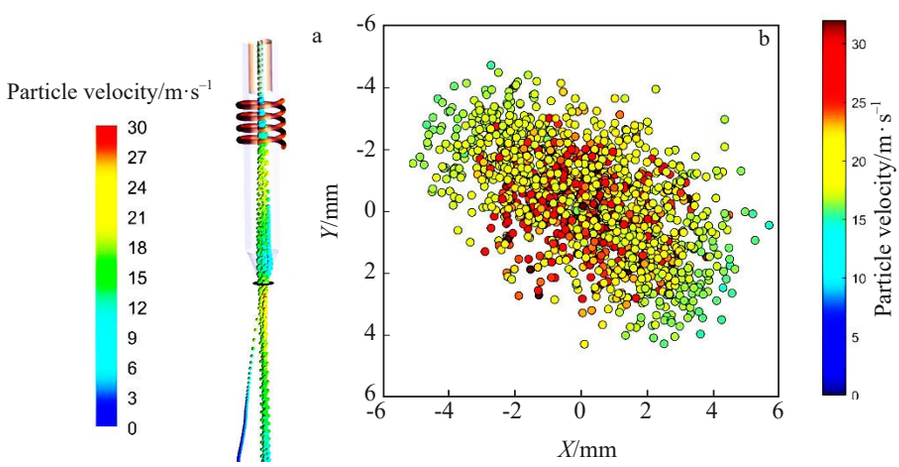

Fig.17 Variation of CeO_2 particle velocity in plasma (a); velocity distribution of CeO_2 particles at nozzle outlet (b)

research, as indicated by the circled area in Fig.19. Therefore, it is unable to form a satisfactory spherical shape. This experiment result is in good agreement with the numerical calculation result. The thermal resistance effect of particles with size larger than 30 μm has a significant impact, resulting in a large temperature difference between the surface and the interior, thus leading to difficulty in complete melting of particles.

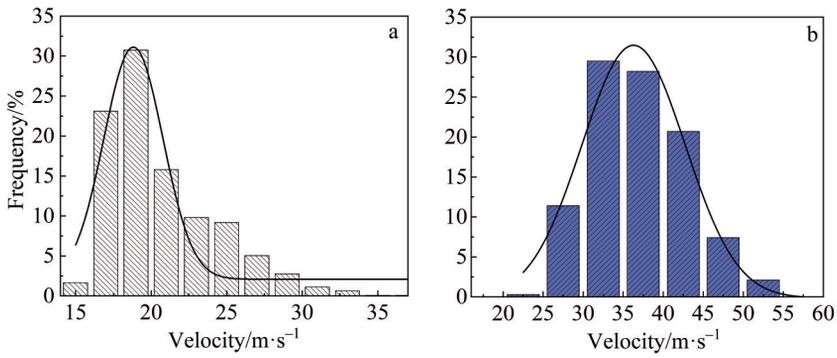

Fig.18 Velocity distribution histograms of CeO_2 particles at nozzle outlet: (a) numerical calculations and (b) experiment measurements

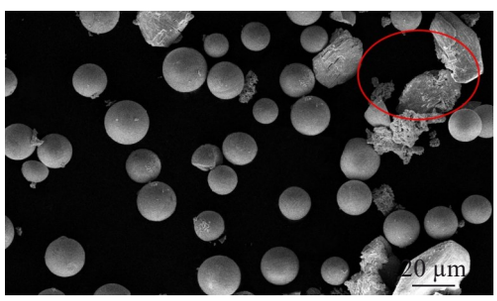

Fig.19 Microstructure of CeO_2 powder processed by RF thermal plasma under experiment conditions

5 Conclusions

1) The in-flight heating process of CeO_2 powder in plasma has three main stages: surface heating, internal heat transfer, and solidification. This heating process is related to a dimensionless parameter, namely Biot number. When the Biot number of the plasma system is close to or larger than 0.1, the influence of thermal resistance must be considered. For the powder with particle size greater than 30 μm, in particular, the thermal resistance effect is more significant when the Biot number is greater than 0.1.

2) Under the specific injection conditions, CeO_2 powder with initial size greater than 30 μm exhibits a more pronounced temperature difference between its surface and center regions, resulting in longer melting time. Especially for the powder with particle size of 50 μm, the surface heating lasts for approximately 5 ms, and the melting lasts for 0.5 ms.

3) Particles with diameter smaller than 30 μm are less affected by thermal resistance effect, and most of them can melt and form good spherical shape. Thermal resistance has a significant impact on large particles (size greater than 30 μm), causing their surfaces to melt and fail to form a spherical shape. The simulation results are in good agreement with the experiment results, indicating the accuracy of the model proposed in this research.

References

1 Wang J J, Hao J J, Guo Z M *et al*. *Rare Metals*[J], 2015, 34(6): 431
2 Zhu H L, Tong H H, Cheng C M *et al*. *International Journal of Refractory Metals and Hard Materials*[J], 2017, 66: 76
3 Vardelle M, Fauchais P, Vardelle A *et al*. *Journal of Thermal Spray Technology*[J], 2001, 10: 267
4 Oh J W, Na H, Cho Y S *et al*. *Nanoscale Research Letters*[J], 2018, 13: 220
5 Samal S. *Journal of Cleaner Production*[J], 2017, 142(4): 3131
6 Cheng Y L, Wang Y K, Chen P *et al*. *International Journal of Agricultural and Biological Engineering*[J], 2014, 7(2): 1
7 Li J, Liu K, Yan S J *et al*. *Waste Management*[J], 2016, 58: 260
8 Nam J S, Park E, Seo J H. *Metals and Materials International*[J], 2020, 26: 491
9 Vlasov V, Shekhovtsov V, Volokitin G *et al*. *Russian Physics Journal*[J], 2018, 61: 708
10 Kim K S, Cota-Sanchez G, Kingston C T *et al*. *Journal of Physics D: Applied Physics*[J], 2007, 40(8): 2375
11 Xiong H B, Zheng L L, Li L *et al*. *International Journal of Heat and Mass Transfer*[J], 2005, 48(25–26): 5121
12 Li X Y, Zhou Z W, Li R Y *et al*. *Plasma Science and Technology*[J], 2023, 25(5): 055504
13 Chen X, Pfender E. *Plasma Chemistry and Plasma Processing*[J], 1983, 3: 351
14 Zhu H L, Li X Y, Chen Q. *Journal of Materials Engineering and Performance*[J], 2022, 31: 6606
15 Wan Y P, Prasad V, Wang G X *et al*. *Journal of Heat Transfer*[J], 1999, 121(3): 691
16 Wan Y P, Fincke J, Sampath S *et al*. *International Journal of Heat and Mass Transfer*[J], 2002, 45(5): 1007
17 Westhoff R, Trapaga G, Szekely J. *Metallurgical Transactions B*[J], 1992, 23: 683
18 Chen X, Pfender E. *Plasma Chemistry and Plasma Processing*[J], 1982, 2: 293
19 Tanaka Y, Takeuchi Y, Sakuyama T *et al*. *Journal of Physics D: Applied Physics*[J], 2007, 41: 025203
20 Wang Y C, Fu Z Y. *Materials Science and Engineering B*[J], 2002, 90(1–2): 34

21 Vardelle A, Vardelle M, Fauchais P. *Plasma Chemistry and Plasma Processing*[J], 1982, 2: 255
22 Kim J, Kang K, Yoon S *et al*. *Surface and Coatings Technology*[J], 2011, 205(8–9): 3020
23 Chen H. *Materials Characterization*[J], 2018, 136: 444
24 Jin M, Wu X, Shao W *et al*. *Ceramics International*[J], 2022, 48(14): 20639
25 Lee Y C, Chyou Y P, Pfender E. *Plasma Chemistry and Plasma Processing*[J], 1985, 5: 391
26 Bourdin E, Fauchais P, Boulos M. *International Journal of Heat and Mass Transfer*[J], 1983, 26(4): 567
27 Rehmet C, Cao T F, Cheng Y. *Plasma Sources Science and Technology*[J], 2016, 25(2): 025011
28 Zhen D, Cao Y G, Ma C Y *et al*. *Rare Metal Materials and Engineering*[J], 2017, 46(2): 333
29 Zhu Hailong, Li Xueying, Tong Honghui. *Acta Physica Sinica*[J], 2021, 70(15): 155202 (in Chinese)
30 Bernardi D, Colombo V, Ghedini E *et al*. *Optical and Plasma Physics*[J], 2004, 28: 423
31 Xue S W, Proulx P, Boulos M I. *Journal of Physics D: Applied Physics*[J], 2001, 34: 1897
32 Holik E F. *Simulation Results of an Inductively-Coupled RF Plasma Torch in Two and Three Dimensions for Producing A Metal Matrix Composite for Nuclear Fuel Cladding*[D]. College Station: Texas A&M University, 2010
33 Furukawa R, Tanaka Y, Nakano Y *et al*. *Journal of Physics D: Applied Physics*[J], 2022, 55(4): 044001
34 ANSYS FLUENT 16 Tutorial Guide[EB]. 2016
35 Li H P, Xi C. *Plasma Chemistry and Plasma Processing*[J], 2002, 22: 27
36 Boulos M I, Fauchais P L, Pfender E. *Handbook of Thermal Plasmas*[M]. Cham: Springer International Publishing, 2023
37 Voile V, Prakash C. *International Journal Heat Mass Transfer*[J], 1987, 30(8): 1709
38 Zhang G H, Fan Y B, Yang R S *et al*. *Powder Technology*[J], 2022, 412: 117982
39 Bailey A, Balachandran W, Williams T. *Journal of Aerosol Science*[J], 1983, 14(1): 39
40 Mendoza G N Y, Morsli M E, Proulx P. *Journal of Thermal Spray Technology*[J], 2008, 17: 533
41 Onda K, Tanaka Y, Akashi K *et al*. *Journal of Physics D: Applied Physics*[J], 2020, 53(32): 325201
42 Bourdin E, Fauchais P, Boulos M. *International Journal of Heat and Mass Transfer*[J], 1983, 26(4): 567
43 Bernardi D, Colombo V, Ghedini E *et al*. *Pure and Applied Chemistry*[J], 2005, 77(2): 359
44 Li M X, Zhang C H, Liu Y *et al*. *Materials Science and Engineering*[J], 2013, 52: 042006
45 Zhang D, Ye K, Liang F *et al*. *Science China Technological Sciences*[J], 2021, 64: 1074
46 Jin X Y, Zhao P, Zeng M H *et al*. *Journal of Thermal Spray Technology*[J], 2023, 32: 162

考虑热阻效应下的氧化铈粉末在射频热等离子体中的飞行加热过程

苏　毅[1,2]，刘睿喆[1]，Ahmad Hilal[1]，赵　鹏[2]，靳兴月[2]，朱海龙[3]
(1. 山西大学 理论物理研究所，山西 太原 030006)
(2. 中国科学院 合肥物质科学研究院 等离子体物理研究所，安徽 合肥 230031)
(3. 山西大学 物理与电子工程学院，山西 太原 030006)

摘　要：对二氧化铈（CeO_2）粉体的飞行加热过程进行了实验和数值模拟研究。在实验中，将CeO_2粉末（平均粒径30 μm）注入射频氩等离子体中，并使用DPV-2000监测仪测量温度。此外，提出了一种结合氩气等离子体中粉末飞行加热的电磁、热流和传热模型。研究了不同粒径的CeO_2粉体的熔化过程以及在热阻作用下的熔融过程。结果表明，CeO_2粉末颗粒的加热过程包括3个主要阶段，其中一个阶段与一个称为Biot数的无量纲参数有关。当Biot数≥0.1时，热阻显著增大，尤其对于较大的粉体。预测的颗粒出口温度（1800~2880 K）与实验结果吻合较好。

关键词：射频热等离子体；热阻效应；加热过程；Biot数

作者简介：苏 毅，男，2000年生，硕士，山西大学理论物理研究所，山西 太原 030006，E-mail：2817764459@qq.com